Chapter

Plasmonic Excitations in Carbon Nanostructures: Carbon Nanotubes Vs. Graphene

Pablo Martín-Luna and Javier Resta-López

Abstract

The interactions of charged particles with carbon nanotubes (CNTs) and graphene layers may excite plasmonic modes in the two-dimensional electron gas that constitute these shells. It has recently been proposed that plasmonic excitations could serve as an innovative approach to short-wavelength, high-gradient particle acceleration. It may transform current particle acceleration techniques and lead to new developments in high-energy physics and related disciplines. In this chapter, we compare the excited wakefields created by a charged particle traveling along a CNT and between two graphene layers. We use a theory based on a linearized hydrodynamic model in conjunction with the Poisson's equation to describe the electronic excitations produced by a fast point-like charge. In this model, surface plasmonic excitations are described by treating the electron gas as a two-dimensional plasma with additional terms in the fluid momentum equation arising from specific solid-state properties of the gas. Analytical expressions of the excited wakefields are derived that, in the case of a single-walled CNT, may be related to the resonant frequencies obtained from the dispersion relation. The dependence of the wakefields on model parameters, such as particle velocity, tube aperture, distance between graphene layers, friction parameter, and surface density, is analyzed.

Keywords: plasmonic excitations, wakefields, carbon nanotubes (CNTs), graphene, hydrodynamic model

1. Introduction

Particle accelerators significantly influence science, industry, and the economy. Traditional accelerators rely on RF technology, but their gradients are restricted to around 100 MV/m due to a phenomenon known as surface RF breakdown [1, 2]. Several alternative approaches are being explored to overcome this limitation, including dielectric laser accelerators and wakefield accelerators [3–7], as well as plasma-based accelerators [8–12]. During the 1980s and 1990s, T. Tajima and others [13–15] proposed solid-state wakefield acceleration using crystals as a potential technique to achieve acceleration gradients on the order of TV/m. In Tajima's initial proposal [13], a longitudinal wakefield is generated by high-energy ($\sim$40 keV) X-rays, which are injected into a crystal lattice at the Bragg angle, producing the Borrmann-Campbell

 IntechOpen

effect [16, 17]. Similarly, ultrashort charged particle bunches can excite electric wakefields, converting the energy loss of the driving bunch into an energy gain for a properly injected witness bunch. However, the angstrom-sized channels of natural crystals limit beam intensity acceptance and increase the dechanneling rate.

In this context, carbon-based nanostructures are considered promising candidates for achieving extremely high gradients because of their exceptional thermal, mechanical, and electronic properties. For example, studies have experimentally shown the transport of 2 MeV He^{+} ions [18] and 300 keV electrons [19] through carbon nanotubes (CNTs). As a result, CNTs can create wider channels in two dimensions and achieve longer dechanneling lengths than natural crystals [20, 21]. Therefore, carbon nanostructures, including CNTs [22–24] and graphene layers [25, 26], are currently under investigation for wakefield acceleration.

The collective oscillation of the free-electron gas (often referred to as plasmons) on carbon nanostructure surfaces (e.g., CNTs or graphene layers) can be responsible for the excitation of wakefields. This wake effect is generated due to the interaction between the driving bunch and the free electrons within these carbon nanostructures. The electronic excitations on CNTs and graphene layers have been theoretically studied employing different approaches, for example, hydrodynamic models [27–38], kinetic models [39–42], and molecular dynamics simulations [43, 44].

In this chapter, we have adopted the linearized hydrodynamic model (LHM) to derive analytical expressions of the excited wakefields in multi-walled CNTs (MWCNTs) and parallel graphene layers. In particular, a detailed study has been conducted on the wakefields excited and the stopping power induced by a proton, comparing a single-walled CNT with a radius of a and two graphene sheets separated by a distance of $2a$. The LHM is chosen for its simplicity and its excellent concordance with the dielectric formalism in the random-phase approximation [28].

This chapter is organized as follows. Section 2 reviews the LHM for multi-layer CNTs and graphene layers, providing general expressions for both longitudinal and transverse wakefields excited by the interaction with a charged particle. Section 3 analyzes the dependence of the wakefields and the stopping power on model parameters, comparing a CNT with two graphene layers. Finally, a summary of the findings of this study is presented in Section 4. Atomic units are used throughout the manuscript, unless otherwise indicated.

2. Linearized hydrodynamic model

In this section, the LHM is used to describe excitations produced by a single charged particle on carbon nanostructure surfaces, for example, MWCNTs or graphene layers. Within this framework, the delocalized electrons of the carbon ions are considered as a free-electron gas distributed uniformly over the surface (considered infinitesimally thin), with the homogeneous density per unit area n_0. We consider that a driving point-like charge Q is moving parallel to the z-axis with a constant velocity v, that is, with coordinates $\mathbf{r}_0(t) = (x_0, y_0, vt)$, neglecting energy losses. The homogeneous electron gas will be perturbed by the driving charge Q, producing a perturbation in the homogeneous electron gas on the surfaces, which can be regarded as charged fluids (confined to the surfaces) with velocity fields $\mathbf{u}_j(\mathbf{r}_j, t)$ and surface density $n(\mathbf{r}_j, t) = n_0 + n_j(\mathbf{r}_j, t)$, where $\mathbf{r}_j$ are the coordinates of a general point at the jth surface and $n_j(\mathbf{r}_j, t)$ is its perturbed density per unit area. In the LHM, $\mathbf{u}_j$ and n_j are considered relatively small perturbations. For the analysis of wakefield dynamics, ionic motion can be neglected [45, 46], since the timescale for ionic movement is much slower than that of electrons, owing to the significantly larger mass of carbon ions compared to electrons.

In the LHM, electronic excitations on the surfaces are described by the continuity equation and the non-relativistic momentum-balance equation at each surface:

$$\frac{\partial n_j(\mathbf{r}_j,t)}{\partial t} + n_0 \nabla_j \cdot \mathbf{u}_j(\mathbf{r}_j,t) = 0, \tag{1}$$

$$\frac{\partial \mathbf{u}_j(\mathbf{r}_j,t)}{\partial t} = \nabla_j \Phi(\mathbf{r}_j,t) - \frac{\alpha}{n_0}\nabla_j n_j(\mathbf{r}_j,t) + \frac{\beta}{n_0}\nabla_j\left[\nabla_j^2 n_j(\mathbf{r}_j,t)\right] - \gamma \mathbf{u}_j(\mathbf{r}_j,t), \tag{2}$$

where we have retained only the first-order terms in n_j and $\mathbf{u}_j$. In these equations, ∇_j differentiates only tangentially to the jth surface and Φ is the electric scalar potential. The sum of four different contributions is considered in Eq. (2). The first term on the right-hand side represents the force applied to the electrons on the jth surface due to the tangential component of the electric field. The total electric potential is the solution to the Poisson equation in free space and can be written as $\Phi = \Phi_0 + \Phi_{\text{ind}}$, where $\Phi_0 = \frac{Q}{|\mathbf{r}-\mathbf{r}_0|}$ is the Coulomb potential produced by the driving charge, and Φ_{ind} is the potential resulting from the perturbation of the electron fluids:

$$\Phi_{\text{ind}}(\mathbf{r},t) = -\sum_j \int \mathrm{d}^2\mathbf{r}_j \frac{n_j(\mathbf{r}_j,t)}{\left\|\mathbf{r}-\mathbf{r}_j\right\|}. \tag{3}$$

The second and third terms correspond to components of the internal interaction force within the electron gas. Specifically, the second term accounts for potential coupling with acoustic modes with $\alpha = v_F^2/2$ ($v_F = (2\pi n_0)^{1/2}$ is the Fermi velocity of the two-dimensional gas), while the third term describes single-electron excitations in the electron gas with $\beta = 1/4$. The final term represents a frictional force on the electrons resulting from scattering with the charges of the ionic lattice, where γ denotes the friction coefficient. Additionally, it serves as a phenomenological parameter to describe the broadening of the plasmon resonance in the excitation spectra of various materials [47].

2.1 Carbon nanotubes

In this case, we consider an MWCNT composed of N concentric cylinders with radii $a_1 < a_2 < \cdots < a_N$ [48], as illustrated in **Figure 1**.

Thus, in Eqs. (1)–(3), we use cylindrical coordinates, and, consequently, $\nabla_j = \hat{\boldsymbol{\varphi}}\frac{1}{a_j}\frac{\partial}{\partial\varphi} + \hat{\mathbf{z}}\frac{\partial}{\partial z}$, $\mathbf{r}_j = (a_j, \varphi, z)$, $\mathrm{d}^2\mathbf{r}_j = a_j \mathrm{d}\varphi \mathrm{d}z$ and the position of the driving particle is $\mathbf{r}_0(t) = (r_0, \varphi_0, vt)$. Eqs. (1)–(3) can be solved by performing a Fourier-Bessel (FB) transform, whose definition for an arbitrary function f is:

$$f(\varphi,z,t) = \sum_{m=-\infty}^{\infty}\int_{-\infty}^{\infty}\frac{\mathrm{d}k}{(2\pi)^2}\int_{-\infty}^{\infty}\frac{\mathrm{d}\omega}{2\pi}\mathrm{e}^{ikz+im\varphi-i\omega t}\tilde{f}(m,k,\omega). \tag{4}$$

The FB transform of the Coulomb potential created by the driving point-like charge and the induced potential are given, respectively, by [24]:

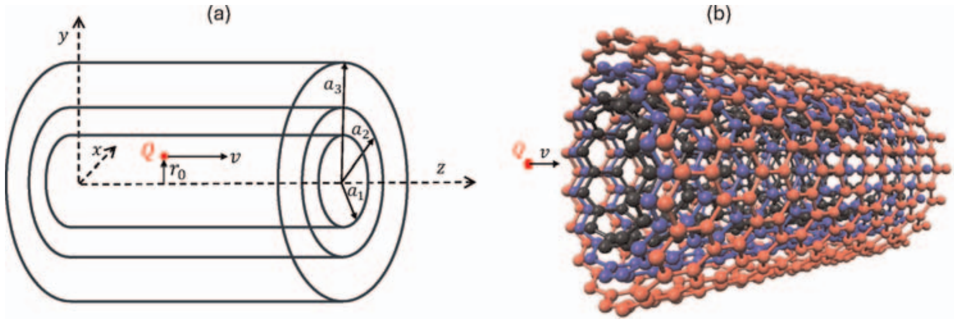

Figure 1.
(a) Schematic of a charge Q moving parallel to the z-axis inside an MWCNT with N = 3 cylinders. (b) Schematic of the hexagonal lattice of a triple-walled CNT.

$$\tilde{\Phi}_0(r, m, k, \omega) = 2\pi Q g(r, r_0; m, k)\delta(\omega - kv)e^{-im\varphi_0}, \tag{5}$$

$$\tilde{\Phi}_{\text{ind}}(r, m, k, \omega) = -\sum_{j=1}^{N} g(r, a_j; m, k) a_j \tilde{n}_j(m, k, \omega), \tag{6}$$

where δ is the Dirac delta, $g(r, r'; m, k) \equiv 4\pi I_m(k|r_{\min}|)K_m(k|r_{\max}|)$ with $r_{\min} = \min(r, r')$, $r_{\max} = \max(r, r')$ and $I_m(x)$ and $K_m(x)$ are the modified Bessel functions of integer order m.

After eliminating $\mathbf{u}_j$ in Eq. (2) by using the continuity equation and applying the FB definition, the FB transform of the perturbed densities can be calculated by solving the system of N coupled linear equations:

$$S_j(m, k, \omega)\tilde{n}_j(m, k, \omega) - \sum_{l=1}^{N} G_{jl}(m, k)\tilde{n}_l(m, k, \omega) = B_j(m, k, \omega), \tag{7}$$

where the following functions have been defined:

$$S_j(m, k, \omega) = \omega(\omega + i\gamma) - \alpha\left(k^2 + m^2/a_j^2\right) - \beta\left(k^2 + m^2/a_j^2\right)^2, \tag{8}$$

$$G_{jl}(m, k) = n_0 a_l\left(k^2 + m^2/a_j^2\right)g(a_j, a_l; m, k), \tag{9}$$

$$B_j(m, k, \omega) = -n_0\left(k^2 + m^2/a_j^2\right)\tilde{\Phi}_0(a_j, m, k, \omega). \tag{10}$$

It is worth noting that Eq. (7) can be expressed as the following matrix equation:

$$M\vec{\tilde{n}} = \vec{B}, \qquad M_{jj} = S_j - G_{jj}, \quad M_{ij} = -G_{ij} \quad (i \neq j). \tag{11}$$

Therefore, the resonant frequencies of the collective excitations in the electron fluids can be obtained by solving the eigenvalue equation $\det(M) = 0$ for $\gamma = 0$. Once the FB of the perturbed densities has been obtained, the induced potential can be calculated as:

$$\Phi_{\text{ind}}(\mathbf{r}, t) = \frac{2}{(2\pi)^3}\sum_{m=-\infty}^{+\infty} e^{im\varphi}\int_0^{+\infty} \text{Re}\left[\tilde{\Phi}_{\text{ind}}(r, m, k, kv)e^{ik\zeta}\right]dk, \tag{12}$$

where $\tilde{\Phi}_{\text{ind}}$ can be obtained using Eq. (6) and the comoving coordinate $\zeta = z - vt$ has been defined. The induced longitudinal and transverse wakefields can be determined by calculating the corresponding partial derivatives: $W_z = -\partial_z \Phi_{\text{ind}}$ and $W_r = -\partial_r \Phi_{\text{ind}}$.

If we consider a single-walled CNT with radius $a \equiv a_1$, the FB transform of the perturbed density can be obtained from Eq. (7) as:

$$\tilde{n}_1(m,k,\omega) = \frac{-2\pi Q n_0 \left(k^2 + m^2/a^2\right) g(a, r_0; m, k) \delta(\omega - kv) e^{-im\varphi_0}}{D_m(k,\omega)}, \tag{13}$$

with $D_m(k,\omega) = \omega(\omega + i\gamma) - \omega_m^2(k)$, where

$$\omega_m^2(k) = \alpha\left(k^2 + m^2/a^2\right) + \beta\left(k^2 + m^2/a^2\right)^2 + \Omega_p^2 a^2\left(k^2 + m^2/a^2\right) K_m(k|a|) I_m(k|a|) \tag{14}$$

are the plasmon dispersion curves and $\Omega_p = \sqrt{4\pi n_0/a}$ is the plasma frequency. The FB transform of the electric potential is $\tilde{\Phi}_{\text{ind}}(r,m,k,\omega) = -g(r,a;m,k)a\tilde{n}_1(m,k,\omega)$. As Eq. (5), implies $\omega = kv$, the condition for plasma resonance is obtained when $k_m v = \omega_m(k_m)$ (i.e., when $D_m(k_m, k_m v) = 0$ for $\gamma \to 0^+$). It is worth noting that the wakefields can be approximately calculated analytically in terms of the roots k_m if $\gamma \to 0^+$ [23, 48].

2.2 Graphene layers

In this case, we consider N parallel graphene layers at planes $y_1 < y_2 < \cdots < y_N$ [26], as illustrated in **Figure 2**.

Hence, in Eqs. (1)–(3), we use Cartesian coordinates and, consequently, $\nabla_j = \hat{\mathbf{x}}\frac{\partial}{\partial x} + \hat{\mathbf{z}}\frac{\partial}{\partial z}$, $\mathbf{r}_j = \left(x, y_j, z\right)$, and $\mathrm{d}^2\mathbf{r}_j = \mathrm{d}x\mathrm{d}z$. The LHM can be solved similarly to the case of MWCNTs, although in the present case we have to use a Fourier transform with respect to coordinates in the xz-plane, $\mathbf{R} = (x,z) \to \mathbf{k} = (k_x, k_z)$, and time, $t \to \omega$, which is defined by

$$A(\mathbf{R}, y, t) = \frac{1}{(2\pi)^3} \int \tilde{A}(\mathbf{k}, y, \omega) e^{-i(\omega t - \mathbf{k}\cdot\mathbf{R})} d^2\mathbf{k} d\omega. \tag{15}$$

The Fourier transform of the electric potential created by the driving charge $\tilde{\Phi}_0$ and the induced electric potential created by the graphene layers $\tilde{\Phi}_{\text{ind}}$ are, respectively,

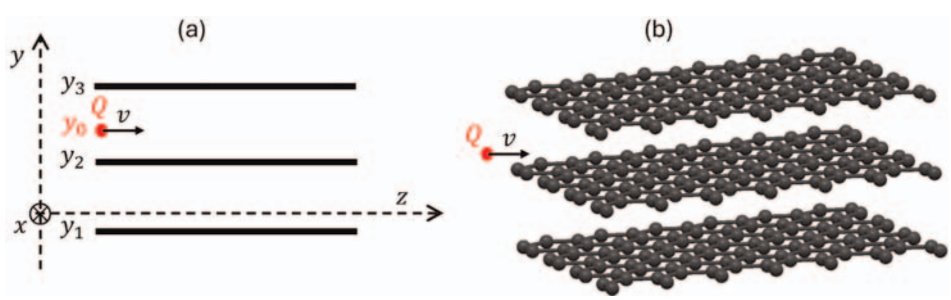

Figure 2.
(a) Schematic of a charge Q moving parallel to the z-axis in a system with $N = 3$ graphene layers. (b) Schematic of the hexagonal lattice of the graphene layers.

$$\tilde{\Phi}_0(\mathbf{k}, y, \omega) = \frac{(2\pi)^2 Q\delta(\omega - \mathbf{k}\cdot\mathbf{v})}{k} e^{-k|y-y_0|}, \tag{16}$$

$$\tilde{\Phi}_{\text{ind}}(\mathbf{k}, y, \omega) = -\sum_{j=1}^{N} \frac{2\pi}{k} \tilde{n}_j(\mathbf{k}, \omega) e^{-k|y-y_j|}, \tag{17}$$

where we have defined $k = \sqrt{k_x^2 + k_z^2}$. If the continuity equation is utilized to eliminate $\mathbf{u}_j$ in Eq. (2) and the Fourier transform definition is applied, Eq. (15), the Fourier transform of the perturbed densities is related by the system of N coupled linear equations:

$$S_j(\mathbf{k}, \omega)\tilde{n}_j(\mathbf{k}, \omega) - \sum_{l=1}^{N} G_{jl}(\mathbf{k})\tilde{n}_l(\mathbf{k}, \omega) = B_j(\mathbf{k}, \omega), \tag{18}$$

where the following functions are defined:

$$S_j(\mathbf{k}, \omega) = \omega(\omega + i\gamma) - \alpha k^2 - \beta k^4, \tag{19}$$

$$G_{jl}(\mathbf{k}) = 2\pi n_0 k e^{-k|y_j - y_l|}, \tag{20}$$

$$B_j(\mathbf{k}, \omega) = -n_0 k^2 \tilde{\Phi}_0\left(\mathbf{k}, y_j, \omega\right). \tag{21}$$

It is important to note the similarity with the expressions obtained in the MWCNTs case: Eqs. (7)–(10). In particular, Eq. (18) can be expressed as the matrix Eq. (11), and, consequently, the dispersion relations may be obtained by solving the eigenvalue equation $\det(M) = 0$ for $\gamma = 0$. Once the $\tilde{n}_j$ have been obtained by solving Eq. (18), the perturbed densities and the electric potential can be determined by utilizing the definition of the Fourier transform, Eq. (15). In particular, by leveraging the symmetry properties of the real and imaginary parts of $\tilde{n}_j$ in $\mathbf{k}$, the perturbed densities and the induced potential can be expressed as:

$$n_j(\mathbf{R}, y, t) = \frac{4}{(2\pi)^3} \int_0^\infty \int_0^\infty \operatorname{Re}\left[\tilde{n}_j(\mathbf{k}, y, k_z v) e^{ik_z\zeta}\right] \cos(k_x x) dk_x dk_z, \tag{22}$$

$$\Phi_{\text{ind}}(\mathbf{R}, y, t) = \frac{4}{(2\pi)^3} \int_0^\infty \int_0^\infty \operatorname{Re}\left[\tilde{\Phi}_{\text{ind}}(\mathbf{k}, y, k_z v) e^{ik_z\zeta}\right] \cos(k_x x) dk_x dk_z, \tag{23}$$

where the comoving coordinate $\zeta = z - vt$ has been defined, as in the case of an MWCNT. Finally, the induced wakefields can be determined by calculating the corresponding partial derivatives:

$$W_x(\mathbf{R}, y, t) = -\frac{\partial \Phi_{\text{ind}}}{\partial x}, \quad W_y(\mathbf{R}, y, t) = -\frac{\partial \Phi_{\text{ind}}}{\partial y}, \quad W_z(\mathbf{R}, y, t) = -\frac{\partial \Phi_{\text{ind}}}{\partial z}. \tag{24}$$

3. Results and discussion

The objective of this research is to compare the wakefields excited inside a CNT with radius a with those excited between two graphene sheets separated a distance $2a$,

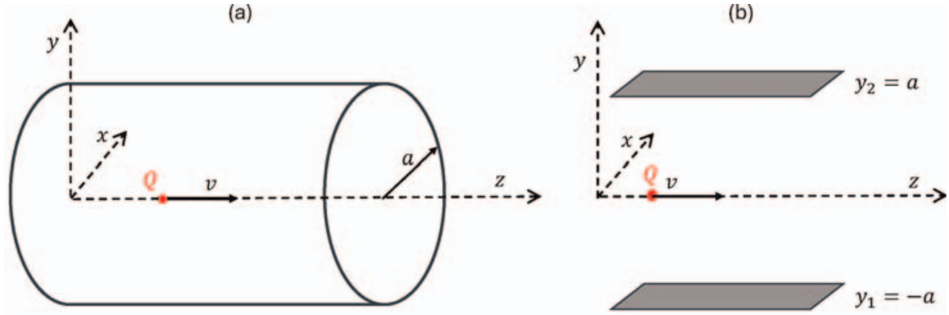

Figure 3.
Schematic of a charge Q moving along the z-axis in (a) a CNT with radius a and (b) two graphene layers at planes $y_1 = -a$ and $y_2 = a$.

that is, the geometries depicted in **Figure 3**. Unless otherwise indicated, it is assumed that the surface electron densities can be approximated by the electron-gas density of a graphite sheet: $n_0 = n_g = 1.53 \times 10^{20} \mathrm{m}^{-2}$ [28, 49].

The roots k_m provided by the plasma resonance are crucial in describing the behavior of the wakefields in a CNT. For this reason, this section begins with a detailed analysis of the dispersion relation of a CNT, comparing it with the dispersion relations of two graphene layers.

3.1 Dispersion relation

Figure 4 shows the dispersion curves $\omega_m(k)$, Eq. (14), for several angular-momentum modes at different CNT radii: (a) $a = 1$ nm and (b) $a = 2$ nm. The resonant wavenumbers k_m occur where the kv line intersects with the dispersion relation $\omega_m(k)$. Consequently, as the driving velocity increases, the resonant wavenumber k_m (if it exists) decreases. The fundamental mode $m = 0$ is the only one that may not satisfy the plasma resonance condition at sufficiently high velocities. From Eq. (14), it is evident that plasma resonance cannot be achieved if $v < \sqrt{\alpha} = v_F/\sqrt{2}$ and that the dispersion curves increase if the surface density n_0 increases. For completeness, the dispersion curves for two graphene layers separated a distance of $2a$

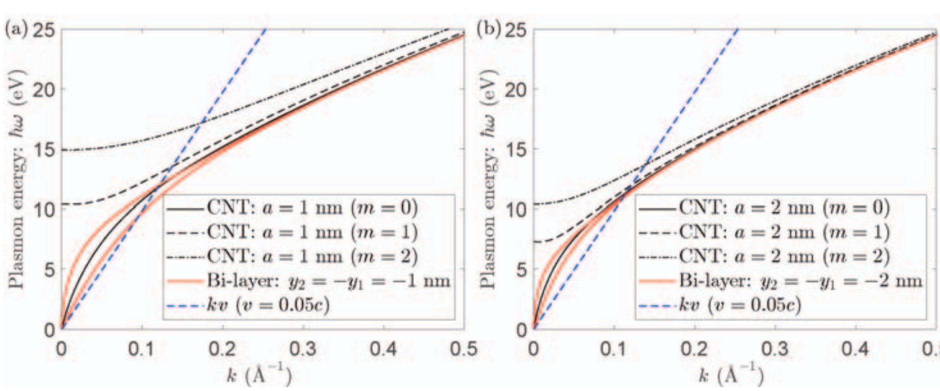

Figure 4.
Plasmon dispersion relations $\omega_m(k)$ for different modes m for a CNT with (a) $a = 1$ nm and (b) $a = 2$ nm. The resonances k_m are the intersection of a kv line (plotted for $v = 0.05c$) with the dispersion curves $\omega_m(k)$. For comparison, we include the dispersion relations for two graphene layers separated by a distance of 2a.

are also included, which are given by $\omega_{\pm}(k) = \sqrt{\omega_1^2 \pm \Delta}$, where $\omega_1^2 = \alpha k^2 + \beta k^4 + 2\pi n_0 k$ is the dispersion relation of a single graphene layer and $\Delta = 2\pi n_0 k e^{-k|y_1 - y_2|}$ describes the electrostatic interaction between both layers. It can be observed that they resemble the fundamental mode $\omega_0(k)$ of the CNT, especially as a increases because the interaction term Δ decreases exponentially with the separation between layers.

3.2 Excited wakefields

For the sake of simplicity, in the following calculations, it is considered that the point-like charged particle is a proton (i.e., $Q = 1$) traveling along the z-axis. Consequently, the fundamental mode $\omega_0(k)$ is the only mode that contributes to the wakefield excitation in the CNT. The integrals in Eqs. (22) and (23) require a finite value of γ for proper convergence. Therefore, a value of $\gamma = 10^{-3}$ a.u.$\approx 4.13 \times 10^{13}$s^{-1} will be used in all cases.

Figure 5 compares the longitudinal wakefield W_z and the transverse wakefield W_y in the $y\zeta$-plane in a CNT and two graphene layers, respectively. It can be seen that the wakefields are similar, although the wakefield intensity is lower in the graphene layers. Additionally, the wakefields diminish rapidly behind the driving particle in the case of the graphene layers, unlike in the case of the CNT, where they hardly decrease. The friction coefficient γ causes an exponential decay of the wakefields behind the driving particle, but a sufficiently small value has been chosen so that it is not noticeable in these cases. The reason for the rapid decay in the graphene layers is that the wakefields spread out in the plane of the layers (i.e., the xz-plane), whereas in the case of the CNT, the wakefields are confined within the tube. To observe this, **Figure 6**

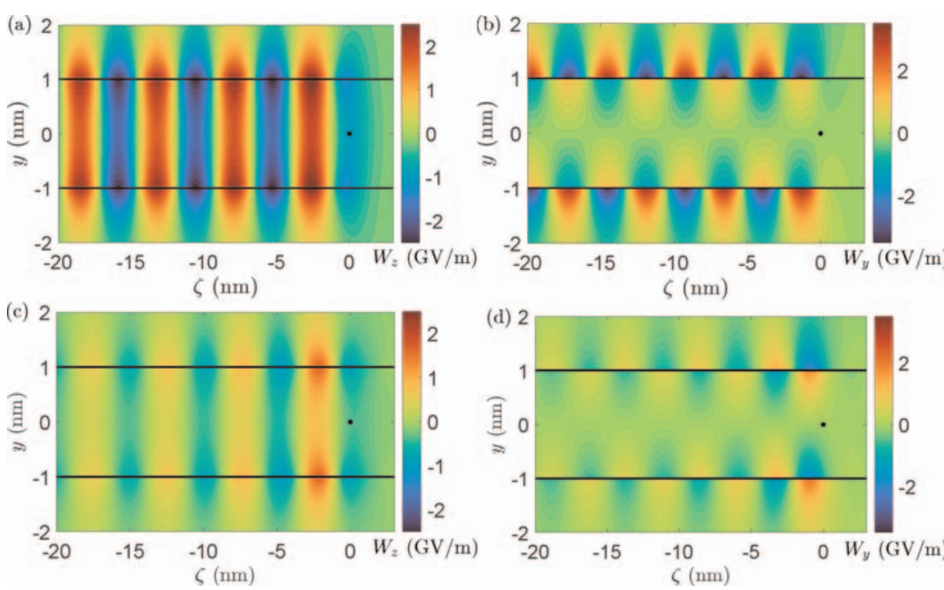

Figure 5.
Induced wakefields (a) W_z and (b) W_y in the $y\zeta$-plane for a proton traveling on the z-axis with a velocity $v = 0.05c$ within a CNT with radius $a = 1$ nm. In (c) and (d), we consider two graphene layers located at $y_2 = -y_1 = a$. In both cases, the friction parameter is $\gamma = 10^{-3}$ a.u.$\approx 4.13 \times 10^{13} s^{-1}$. The wakefield W_x is zero in the $y\zeta$-plane. The proton is indicated with a black point and the CNT wall and the graphene layers with black lines.

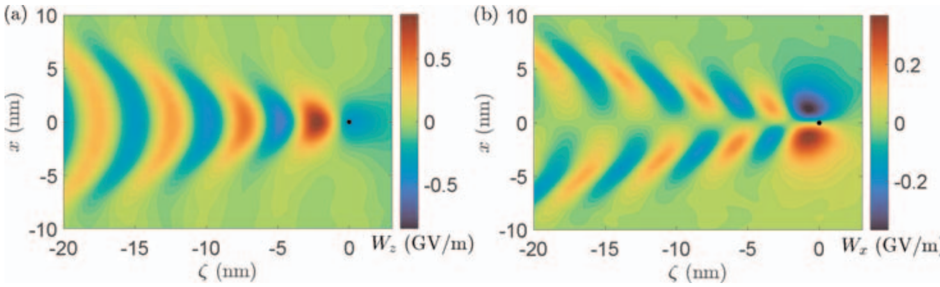

Figure 6.
Induced wakefields (a) W_z and (b) W_x in the $x\zeta$-plane for a proton traveling on the z-axis with a velocity $v = 0.05c$ within two graphene layers located at $y_2 = -y_1 = a$. The wakefield W_y is zero in the $x\zeta$-plane. The proton is indicated with a black point.

depicts the wakefields W_z and W_x in the $x\zeta$-plane in the bi-layer configuration. Due to the cylindrical symmetry of the CNT, the wakefields W_z and W_x in the $x\zeta$-plane are identical to the wakefields W_z and W_y, respectively, in the $y\zeta$-plane, that is, the wakefields depicted in **Figure 5(a)** and **(b)**. This difference in wakefields is highly significant for particle acceleration purposes. In CNTs, there are regions where a witness beam experiences both acceleration and focusing simultaneously. However, in the bi-layer configuration, if acceleration and focusing are achieved in the $y\zeta$-plane ($x\zeta$-plane), then there would be defocusing in the $x\zeta$-plane ($y\zeta$-plane).

For completeness, **Figure 7** shows the perturbed density n_1/n_0 in the CNT and the graphene layer. Due to the symmetry, the perturbed density depends only on ζ in the CNT and $n_1 = n_2$ in the bi-layer configuration. Similar to the wakefields in the $x\zeta$-plane, the perturbed density spreads out in the graphene layers. It is worth noting that the perturbed densities satisfy $n_1 \ll n_0$, as assumed in the linearized hydrodynamic model.

Figure 8 shows the induced longitudinal wakefield W_z in the z-axis in order to study the effect of each parameter: the driving velocity v, the CNT radius a (separation between layers $2a$), and the surface density n_0. It can be observed that the wavelength of the wakefield increases with the velocity, whereas the intensity of the wakefield decreases for low velocities and for high velocities, that is, there is an optimal velocity for which the wakefield intensity is maximum. Moreover, the wavelength of the plasmonic excitations increases with the velocity v. As can be seen in

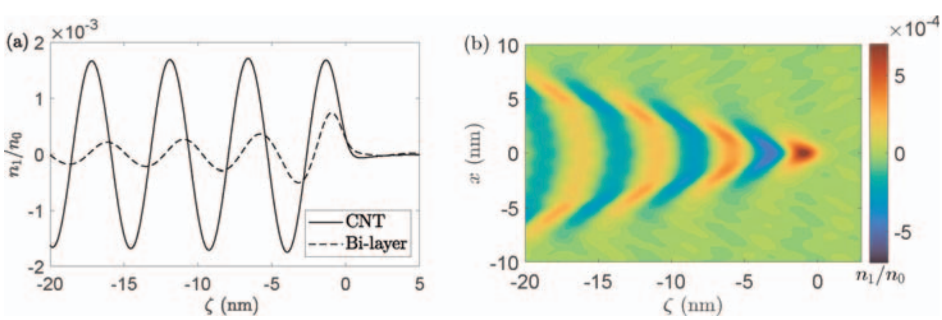

Figure 7.
(a) Normalized perturbed density n_1/n_0 for a proton traveling on the z-axis with a velocity $v = 0.05c$ within a CNT with radius $a = 1$ nm and two graphene layers located at $y_2 = -y_1 = a$. In (b) we show the perturbed density in the layer plane, that is, at $y_1 = -a$. Due to symmetry, the perturbed density in both layers is identical.

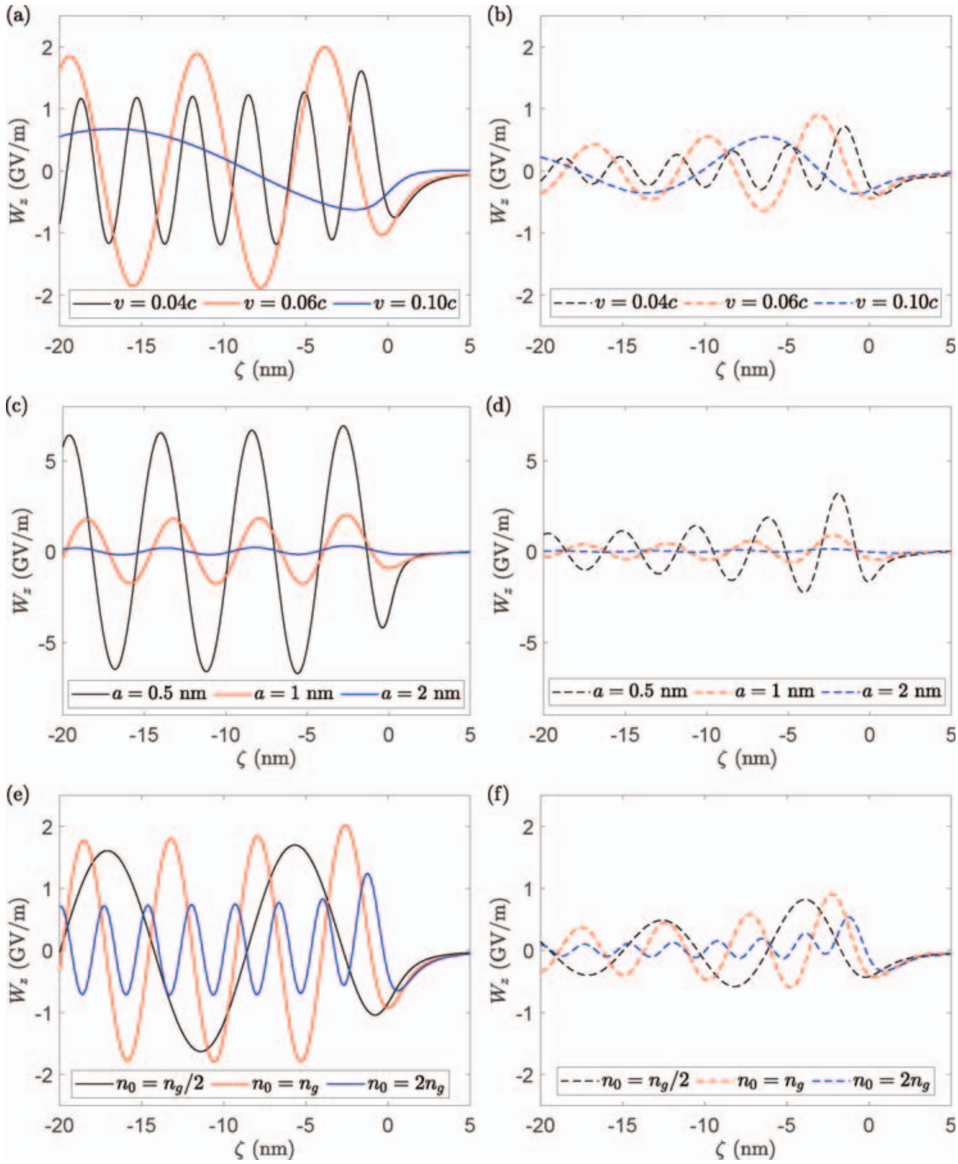

Figure 8.
Longitudinal wakefield W_z along the z-axis for a proton traveling on the z-axis for different (a)-(b) velocities v, (c)-(d) CNT radii a or separation between layers 2a and (e)-(f) surface density n_0. In all cases, unless otherwise indicated in the corresponding legend, the following parameters are used: $v = 0.05c$, a = 1 nm, $n_0 = n_g$. Solid lines indicate the CNT case (left column) and dashed lines the bi-layer configuration (right column).

Figure 8(c) and **(d)**, the intensity of the wakefields increases as a diminishes (this behavior is consistently observed in the graphene layers, but for CNTs the intensity decreases for very small radii; see **Figure 11**). Finally, **Figure 8(e)** and **(f)** illustrate that the intensity of the wakefields decreases for low and high surface densities, that is, there is an optimum density (in this case, $n_0 \approx n_g$). The wavelength of the wakefields decreases with the surface density. The dependence of the wavelength on velocity and surface density can be directly deduced from the dispersion relation. As the velocity decreases (or surface density increases), the value of the resonant wavenumber k_0 increases, leading to a decrease in wavelength ($\lambda \sim 2\pi/k_0$). Finally, it is observed that, in general, CNTs produce more intense wakefields that do not decay rapidly and have longer wavelengths compared to graphene layers.

3.3 Maximum wakefield and stopping power

This section is dedicated to comparing the maximum longitudinal wakefield excited along the z-axis $\left(W_z^{max}\right)$ in the CNT and in the bi-layer configuration. For completeness, we will examine the stopping power, which refers to the energy loss of a channeled particle per unit path length caused by the collective electron excitations. This magnitude can be calculated as

$$S = -QW_z|_{\mathbf{r}=\mathbf{r}_0}, \tag{25}$$

and exhibits a behavior similar to that of the excited longitudinal wakefield amplitude [24]. **Figure 9** depicts W_z^{max} and the stopping power as a function of the driving velocity for different values of a. Both the CNT and the bi-layer configuration exhibit qualitatively similar behavior: W_z^{max} decreases as the parameter a increases. In both cases, the maximum is reached at a similar velocity (slightly lower in the CNT). In the CNT, a larger wakefield (approximately twice as large) can be obtained, but it decreases more rapidly at high velocities compared to the graphene layers. It is also observed that W_z^{max} and the stopping power have a very similar trend, except at very low velocities where W_z^{max} tends to a finite value and the stopping power to zero. In fact, at these very low velocities, no plasmonic excitation (i.e., an oscillating wakefield) occurs, and the wakefield is only generated near the driving particle [35, 36].

Figure 10 shows W_z^{max} and the stopping power as a function of the driving velocity for different surface densities n_0. Again, both configurations (CNT and graphene layers) exhibit qualitatively similar behavior. It is interesting to note that the maximum of W_z^{max} and the stopping power shift to higher velocities with the surface density, although their peak values remain approximately constant.

Finally, **Figure 11** analyzes W_z^{max} and the stopping power as a function of a. It is observed that in graphene layers, these magnitudes increase as the layers are closer together, whereas for CNTs, it exists an optimal radius.

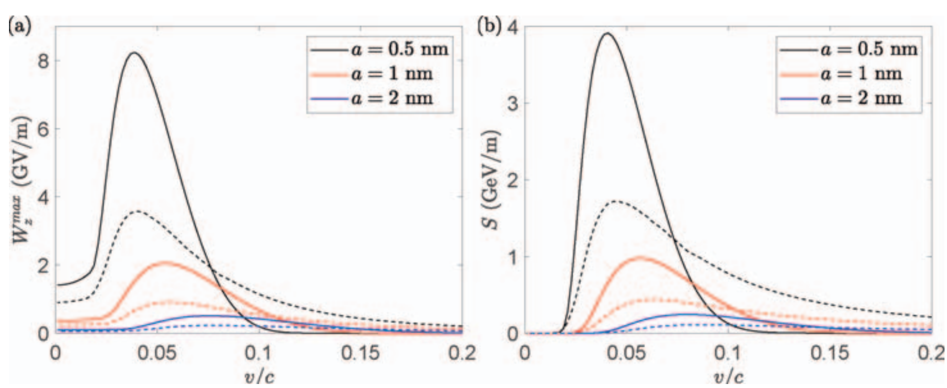

Figure 9.
(a) Maximum longitudinal wakefield W_z^{max} and (b) stopping power as a function of the driving velocity for different values of a. Solid lines indicate the CNT case and dashed lines the bi-layer configuration.

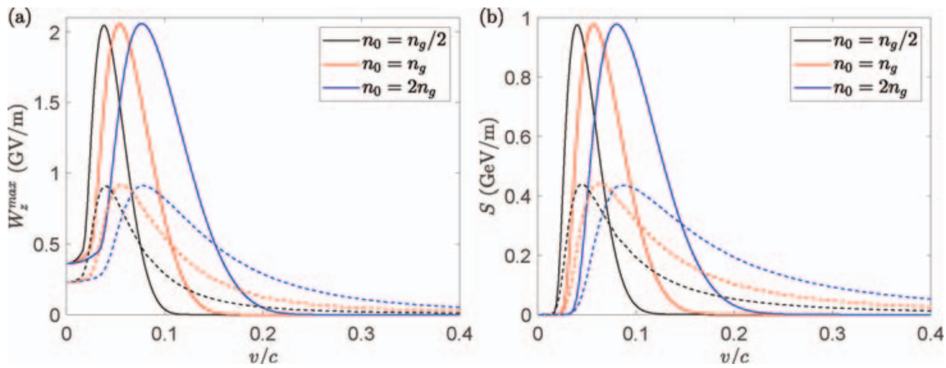

Figure 10.
(a) Maximum longitudinal wakefield W_z^{max} and (b) stopping power as a function of the driving velocity for different values of the surface density n_0 for $a = 1$ nm. Solid lines indicate the CNT case and dashed lines the bi-layer configuration.

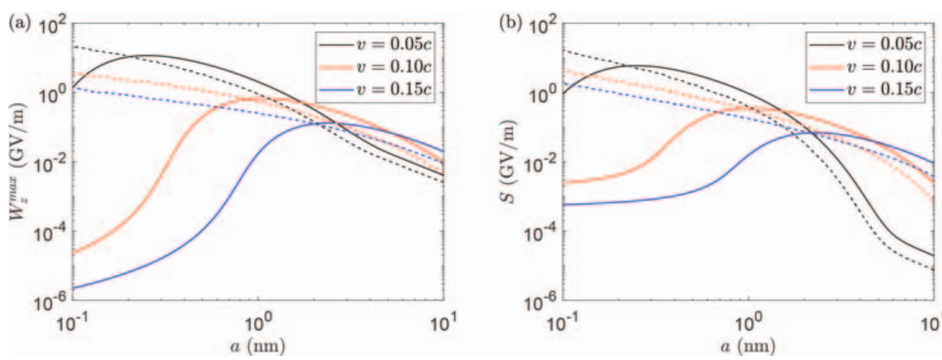

Figure 11.
(a) Maximum longitudinal wakefield W_z^{max} and (b) stopping power as a function of the CNT radius a (layers separated a distance 2a) for different values of the driving velocity. Solid lines indicate the CNT case and dashed lines the bi-layer configuration.

4. Conclusions and outlook

The linear hydrodynamic model has been revisited to derive general expressions for the electric wakefields excited by a point-like charge in carbon nanostructures, in particular MWCNT and parallel graphene layers. The excitation in a CNT with radius a has been compared in detail with that between two graphene layers separated by a distance of $2a$.

As the wakefields of a CNT are closely related to the dispersion relation, the dispersion curves have been initially plotted. It has been observed that the bi-layer configuration exhibits two dispersion curves that resemble the dispersion relation $\omega_0(k)$ of the CNT, especially as a increases.

Subsequently, the excited wakefields have been compared in a specific case. It has been observed that in the plane perpendicular to the graphene layers (i.e., the yz-plane), the fields qualitatively resemble each other, except that the wakefields decay with distance in the bi-layer case. The rapid decay in the graphene layers occurs because the wakefields spread out in the plane of the layers (i.e., the xz-plane), whereas in the case of the CNT, the wakefields are confined within the tube structure.

Thus, a witness beam could experience acceleration and focusing in a CNT, whereas in the graphene layers, it would be focused in one plane and defocused in the perpendicular plane.

Finally, the maximum excited longitudinal wakefield along the z-axis and the stopping power have been studied. These magnitudes exhibit qualitatively similar behavior in both the CNT and the graphene layers, with the exception that in the CNT there is an optimal radius (i.e., a radius that maximizes these magnitudes), whereas in the graphene layers, these magnitudes increase as the separation decreases.

In summary, the excitation of very intense wakefields in carbon nanostructures has been demonstrated, which could pave the way for new applications in particle acceleration or radiation sources.

Acknowledgements

This work has been supported by Ministerio de Universidades (Gobierno de España) under grant agreement FPU20/04958 and the Generalitat Valenciana under grant agreement CIDEGENT/2019/058.

Abbreviations

CNT	carbon nanotube
FB	Fourier-Bessel
LHM	linearized hydrodynamic model
MWCNT	multi-walled carbon nanotube

Author details

Pablo Martín-Luna[1*†] and Javier Resta-López[2*†]

1 Instituto de Física Corpuscular (IFIC), Universitat de València - Consejo Superior de Investigaciones Científicas, Paterna, Spain

2 Instituto de Ciencia de los Materiales (ICMUV), Universidad de Valencia, Valencia, Spain

*Address all correspondence to: pablo.martin@uv.es; javier2.resta@uv.es

† These authors contributed equally.

References

[1] Abe T, Kageyama T, Sakai H, Takeuchi Y, Yoshino K. Breakdown study based on direct in situ observation of inner surfaces of an RF accelerating cavity during a high-gradient test. Physical Review Accelerators and Beams. 2016;**19**:102001. DOI: 10.1103/PhysRevAccelBeams.19.102001

[2] Shao J. Investigations on rf Breakdown Phenomenon in High Gradient Accelerating Structures. Singapore: Springer; 2018. DOI: 10.1007/978-981-10-7926-9

[3] Thompson MC, Badakov H, Cook AM, Rosenzweig JB, Tikhoplav R, Travish G, et al. Breakdown limits on Gigavolt-per-meter electron-beam-driven Wakefields in dielectric structures. Physical Review Letters. 2008;**100**:214801. DOI: 10.1103/PhysRevLett.100.214801

[4] Breuer J, Hommelhoff P. Laser-based acceleration of nonrelativistic electrons at a dielectric structure. Physical Review Letters. 2013;**111**:134803. DOI: 10.1103/PhysRevLett.111.134803

[5] Peralta E, Soong K, England R, Colby E, Wu Z, Montazeri B, et al. Demonstration of electron acceleration in a laser-driven dielectric microstructure. Nature. 2013;**503**(7474):91-94. DOI: 10.1038/nature12664

[6] England RJ, Noble RJ, Bane K, Dowell DH, Ng CK, Spencer JE, et al. Dielectric laser accelerators. Reviews of Modern Physics. 2014;**86**:1337-1389. DOI: 10.1103/RevModPhys.86.1337

[7] O'Shea B, Andonian G, Barber S, Fitzmorris K, Hakimi S, Harrison J, et al. Observation of acceleration and deceleration in gigaelectron-volt-per-metre gradient dielectric wakefield accelerators. Nature Communications. 2016;**7**(1):1-7. DOI: 10.1038/ncomms12763

[8] Tajima T, Dawson JM. Laser electron accelerator. Physical Review Letters. 1979;**43**:267-270. DOI: 10.1103/PhysRevLett.43.267

[9] Chen P, Dawson JM, Huff RW, Katsouleas T. Acceleration of electrons by the interaction of a bunched electron beam with a plasma. Physical Review Letters. 1985;**54**:693-696. DOI: 10.1103/PhysRevLett.54.693

[10] Gordon D, Tzeng KC, Clayton CE, Dangor AE, Malka V, Marsh KA, et al. Observation of electron energies beyond the linear dephasing limit from a laser-excited relativistic plasma wave. Physical Review Letters. 1998;**80**:2133-2136. DOI: 10.1103/PhysRevLett.80.2133

[11] Leemans WP, Nagler B, Gonsalves AJ, Tóth C, Nakamura K, Geddes CG, et al. GeV electron beams from a centimetre-scale accelerator. Nature Physics. 2006;**2**(10):696-699. DOI: 10.1038/nphys418

[12] Litos M, Adli E, An W, Clarke C, Clayton C, Corde S, et al. High-efficiency acceleration of an electron beam in a plasma wakefield accelerator. Nature. 2014;**515**(7525):92-95. DOI: 10.1038/nature13882

[13] Tajima T, Cavenago M. Crystal x-ray accelerator. Physical Review Letters. 1987;**59**:1440-1443. DOI: 10.1103/PhysRevLett.59.1440

[14] Chen P, Noble RJ. A solid state accelerator. AIP Conference Proceedings. 1987;**156**:222-227. DOI: 10.1063/1.36458

[15] Chen P, Noble RJ. Crystal channel collider: Ultra-high energy and luminosity in the next century. AIP Conference Proceedings. 1997;**398**: 273-285. DOI: 10.1063/1.53055

[16] Borrmann G. Die absorption von röntgenstrahlen im fall der interferenz. Zeitschrift für Physik. 1950;**127**(4): 297-323. DOI: 10.1007/BF01329828

[17] Campbell H. X-ray absorption in a crystal set at the Bragg angle. Journal of Applied Physics. 1951;**22**(9):1139-1142. DOI: 10.1063/1.1700122

[18] Zhu Z, Zhu D, Lu R, Xu Z, Zhang W, Xia H. The experimental progress in studying of channeling of charged particles along nanostructure. In: Dabagov SB, editor. International Conference on Charged and Neutral Particles Channeling Phenomena, Society of Photo-Optical Instrumentation Engineers (SPIE) Conference Series. Vol. 5974. Bellingham, WA: SPIE; 2006. pp. 382-389. DOI: 10.1117/12.640101

[19] Chai G, Heinrich H, Chow L, Schenkel T. Electron transport through single carbon nanotubes. Applied Physics Letters. 2007;**91**(10):103101. DOI: 10.1063/1.2778551

[20] Biryukov VM, Bellucci S. Nanotube diameter optimal for channeling of high-energy particle beam. Physics Letters B. 2002;**542**(1):111-115. DOI: 10.1016/S0370-2693(02)02276-1

[21] Bellucci S, Biryukov VM, Cordelli A. Channeling of high-energy particles in a multi-wall nanotube. Physics Letters B. 2005;**608**(1):53-58. DOI: 10.1016/j.physletb.2005.01.003

[22] Bonatto A, Xia G, Apsimon O, Bontoiu C, Kukstas E, Rodin V, et al. Exploring ultra-high-intensity wakefields in carbon nanotube arrays: An effective plasma-density approach. Physics of Plasmas. 2023;**30**(3):033105. DOI: 10.1063/5.0134960

[23] Martín-Luna P, Bonatto A, Bontoiu C, Xia G, Resta-López J. Excitation of wakefields in carbon nanotubes: A hydrodynamic model approach. New Journal of Physics. 2023;**25**(12):123029. DOI: 10.1088/1367-2630/ad127c

[24] Martín-Luna P, Bonatto A, Bontoiu C, Xia G, Resta-López J. Plasmonic excitations in double-walled carbon nanotubes. Results in Physics. 2024;**60**:107698. DOI: 10.1016/j.rinp.2024.107698

[25] Bonțoiu C, Apsimon O, Kukstas E, Rodin V, Yadav M, Welsch C, et al. TeV/m catapult acceleration of electrons in graphene layers. Scientific Reports. 2023;**13**:1330. DOI: 10.1038/s41598-023-28617-w

[26] Martín-Luna P, Bonatto A, Bontoiu C, Lei B, Xia G, Resta-López J. Plasmonic excitations in graphene layers. arXiv. 2025. Available from: https://arxiv.org/abs/2501.05998

[27] Stöckli T, Bonard JM, Châtelain A, Wang ZL, Stadelmann P. Collective oscillations in a single-wall carbon nanotube excited by fast electrons. Physical Review B. 2001;**64**:115424. DOI: 10.1103/PhysRevB.64.115424

[28] Wang YN, Mišković ZL. Interactions of fast ions with carbon nanotubes: Self-energy and stopping power. Physical Review A. 2004;**69**:022901. DOI: 10.1103/PhysRevA.69.022901

[29] Mowbray DJ, Mišković ZL, Goodman FO, Wang YN. Interactions of fast ions with carbon nanotubes: Two-fluid model. Physical Review B. 2004;**70**:

195418. DOI: 10.1103/PhysRevB.70.195418

[30] Mowbray DJ, Mišković ZL, Goodman FO, Wang YN. Wake effect in interactions of fast ions with carbon nanotubes. Physics Letters A. 2004; **329**(1):94-99. DOI: 10.1016/j.physleta.2004.06.090

[31] Mowbray DJ, Chung S, Mišković ZL, Goodman FO, Wang YN. Dynamic interactions of fast ions with carbon nanotubes. Nuclear instruments and methods in physics research section B: Beam interactions with materials and atoms. Atomic Collisions in Solids. 2005; **230**(1):142-147. DOI: 10.1016/j.nimb.2004.12.032

[32] Chung S, Mowbray DJ, Mišković ZL, Goodman FO, Wang YN. Dynamic interactions of fast ions with multiwalled carbon nanotubes. Radiation Physics and Chemistry. 2007;**76**(3):524-528. DOI: 10.1016/j.radphyschem.2005.09.020

[33] Wei L, Wang YN. Quantum ion-acoustic waves in single-walled carbon nanotubes studied with a quantum hydrodynamic model. Physical Review B. 2007;**75**:193407. DOI: 10.1103/PhysRevB.75.193407

[34] Radović I, Hadžievski L, Bibić N, Mišković ZL. Dynamic-polarization forces on fast ions and molecules moving over supported graphene. Physical Review A. 2007;**76**(4):042901. DOI: 10.1103/PhysRevA.76.042901

[35] Radović I, Borka D. Interactions of fast charged particles with supported two-dimensional electron gas: One-fluid model. Physics Letters A. 2010;**374**(13): 1527-1533. DOI: 10.1016/j.physleta.2010.01.056

[36] Radović I, Borka D. Wake effect in interactions of fast ions with supported two-dimensional electron gas. Nuclear Instruments and Methods in Physics Research Section B: Beam Interactions with Materials and Atoms. 2010;**268**(17): 2649-2654. DOI: 10.1016/j.nimb.2010.06.043

[37] Li CZ, Wang YN, Song YH, Mišković ZL. Interactions of charged particle beams with double-layered two-dimensional quantum electron gases. Physics Letters A. 2014;**378**(22): 1626-1631. DOI: 10.1016/j.physleta.2014.04.007

[38] Borka D, Radović I, Vuković K. Energy loss of charged particles traversing multilayer graphene. Nuclear Instruments and Methods in Physics Research Section B: Beam Interactions with Materials and Atoms. 2015;**347**: 7-10. DOI: 10.1016/j.nimb.2015.01.057

[39] Song YH, Zhao D, Wang YN. Kinetic study on self-energy and stopping power of charged particles moving in metallic carbon nanotubes. Physical Review A. 2008;**78**:012901. DOI: 10.1103/PhysRevA.78.012901

[40] Zhao D, Song YH, Wang YN. Kinetic study on Channelling of protons in metallic carbon nanotubes. Chinese Physics Letters. 2008;**25**(7):2588. DOI: 10.1088/0256-307X/25/7/070

[41] Zhang YY, Sun JZ, Song YH, Mišković ZL, Wang YN. Channeling of protons in single-walled carbon nanotubes based on kinetic and molecular-dynamics treatment. Carbon. 2014;**71**:196-205. DOI: 10.1016/j.carbon.2014.01.030

[42] Fermanian Kammerer C, Méhats F. A kinetic model for the transport of electrons in a graphene layer. Journal of Computational Physics. 2016;**327**: 450-483. DOI: 10.1016/j.jcp.2016.09.010

[43] Zhang YY, Song YH, Radović I, Wang YN, Mišković ZL. Interactions of moving charged particles with triple-walled carbon nanotubes. European Physical Journal D: Atomic, Molecular, Optical and Plasma Physics. 2017;**71**:219. DOI: 10.1140/epjd/e2017-70744-3

[44] Loche P, Ayaz C, Schlaich A, Bonthuis DJ, Netz RR. Breakdown of linear dielectric theory for the interaction between hydrated ions and graphene. The Journal of Physical Chemistry Letters. 2018;**9**(22): 6463-6468. DOI: 10.1021/acs.jpclett.8b02473

[45] Hakimi S, Nguyen T, Farinella D, Lau CK, Wang HY, Taborek P, et al. Wakefield in solid state plasma with the ionic lattice force. Physics of Plasmas. 2018;**25**(2):023112. DOI: 10.1063/1.5016445

[46] Hakimi S, Zhang X, Lau C, Taborek P, Dollar F, Tajima T. X-ray laser Wakefield acceleration in a nanotube. International Journal of Modern Physics A. 2019;**34**(34): 1943011. DOI: 10.1142/S0217751X19430115

[47] Arista NR. Interaction of ions and molecules with surface modes in cylindrical channels in solids. Physical Review A. 2001;**64**:032901. DOI: 10.1103/PhysRevA.64.032901

[48] Martín-Luna P, Resta-López J. Excitation of plasmonic wakefields in multi-walled carbon nanotubes: A hydrodynamic approach. In: Kuznetsov DA, editor. Carbon Nanotubes - Recent Advances, Perspectives and Applications. Rijeka: IntechOpen; 2024. DOI: 10.5772/intechopen.114270

[49] Östling D, Tománek D, Rosén A. Electronic structure of single-wall, multiwall, and filled carbon nanotubes. Physical Review B. 1997;**55**:13980-13988. DOI: 10.1103/PhysRevB.55.13980